Applied Thermal Engineering 255 (2024) 123956

Contents lists available at ScienceDirect

Applied Thermal Engineering

journal homepage: www.elsevier.com/locate/apthermeng

Research Paper

# Experimental investigation on the heat transfer characteristics of loop heat pipe with carbon spheres modified nickel wick

Zhengyuan Ma, Yubo Tan, Zikang Zhang, Wei Liu, Zhichun Liu *

*School of Energy and Power Engineering, Huazhong University of Science and Technology, Wuhan, 430074, China*

ARTICLE INFO

*Keywords:*
Loop heat pipe
Carbon spheres modified nickel wick
Surface modification
Hydrophilic functional groups

ABSTRACT

Loop heat pipe (LHP), as passive heat transfer system, is one of the methods for thermal management of electronic components. To improve the heat transfer performance of LHPs, there is a pressing need for high-performance wicks. In this study, the hydrothermal carbonization method was used to fabricate a carbon spheres modified nickel wick (CSs-Ni-Wick) based on a biporous wick. The physical characteristics of the CSs-Ni-Wick were then analyzed experimentally. This unique CSs-Ni-Wick combined the advantages of large pores for reducing flow resistance and small pores for enhancing capillarity. Furthermore, the CSs-Ni-Wick surface exhibited a higher concentration of hydrophilic functional groups, effectively facilitating the replenishment of subcooled liquid to the vapor–liquid interface and preventing wick drying. Based on these advantages, a flat plate LHP was constructed and subjected to multiple tests in horizontal condition to evaluate the heat transfer performance of the CSs-Ni-Wick. Experimental results revealed that the LHP achieved a maximum heat load of 140 W (20 W/cm$^2$) and a minimum thermal resistance of 0.357 °C/W, while maintaining the heat source temperature below 85°C. Additionally, the implementation of a micro-carbonized surface increased the density of vaporization cores, facilitating faster vapor nucleation, particularly at low heat loads. This enables vapor to be transferred more quickly from the evaporator to the condenser, leading to a smooth startup in the brass LHP using methanol as the working fluid, characterized by the absence of temperature overshoot or oscillation.

## 1. Introduction

The sustained progression of the electronic information industry is supported by the advancement of electronic component performance. As electronic equipment becomes increasingly complex and integrated, chip devices now generate more waste heat, surpassing previous generations. This increase in the generation of wasted heat results in elevated operational temperatures, leading to a decrease in performance or even failure of the electronic components [1]. Therefore, it is important to employ effective heat dissipation methods to transfer the heat generated during device operation to the external environment, ensuring that the operating temperature remains within an acceptable range. Phase-change cooling technology, utilizing the latent heat of vaporization and condensation of a working fluid to transport waste heat, offers a higher working capacity in comparison to traditional forced-air cooling and single-phase liquid cooling methods. This technology is capable of meeting the heat dissipation requirements of devices that generate high heat flux. As a typical two-phase heat transfer component, the loop heat pipe (LHP) which was proposed by Maydanik in 1972 [2], possess several advantages, including high heat transfer capacity [3], high heat transfer coefficient [4] and no additional power consumption [5]. Consequently, LHPs have found widespread applications in aerospace [6,7], electric vehicle [8,9], solar collector [10,11], high-power electronic components [12,13], seawater desalination [14,15] and etc.

A LHP system comprises several key components: the evaporator, the condenser, the working fluid, the wick, the vapor line, and the liquid line. Generally, the vapor line and the liquid line are smooth pipes, so the optimization of LHPs primarily focuses on the evaporator design, the condenser design, the selection of the working fluid, and the wick design. Firstly, it is important to optimize the structure of the evaporator and condenser. Nakatsugawa et al. [16] utilized a short-pulse laser technique to engrave grid-like grooves onto the evaporator's heat-absorbing surface. Their investigation revealed that the macroscopic contact angle of ethanol on the micro-grooved plate was a mere 0°, indicative of excellent wetting properties. By implementing micro-grooves on the heating surface, the heat transfer coefficient could be amplified by factors of 3.8, 2.4, and 1.2 for vapor groove widths of 1.0

* Corresponding author at: 318 Power Building, 1037 Luoyu Road, Hongshan District, Wuhan 430074, China.
*E-mail address:* zcliu@hust.edu.cn (Z. Liu).

https://doi.org/10.1016/j.applthermaleng.2024.123956
Received 27 December 2023; Received in revised form 30 May 2024; Accepted 15 July 2024
Available online 18 July 2024

mm, 0.5 mm, and 0.2 mm, respectively. Additionally, the maximum heat flux was increased by factors of 1.8, 1.4 and 1.1, respectively. Yang et al. [17] designed an evaporator structure with longitudinal liquid replenishment and investigated the influence of the position of the heating surface and the distance of the compensation chamber(CC) on the rectangular evaporator. The results revealed that as the proximity of the heating surface to the CC decreased, the thermal resistance of the LHP reduced significantly. Xiong et al. [18] introduced an innovative approach by sintering a 1 mm thick layer of copper powder inside the CC. This modification aimed to enhance the liquid delivery capacity of the wick. Consequently, the LHP demonstrated remarkable operational performance in positive gravity directions, especially +90°, and the operating temperature was 95.96 °C at the highest heat load of 750 W. Fukushima et al. [19] produced grooves on the CC side that were aligned with the wick structure. The design led to the creation of a more expansive flow passage, which in turn reduced the pressure drop within the wick and increased the CC volume. The resultant micro-LHP achieved a maximum heat load of 11 W and a minimum thermal resistance of 1.21 °C/W. Han et al. [20] coupled a high thermal conductivity heat dissipation material with a plate-type evaporator, resulting in a decrease of peak temperatures by 3.8 °C to 7.7 °C across a wide range of thermal loads from 80 W to 120 W. This was achieved by incorporating a graphene-copper foil hybrid heat sink. Du et al. [21] removed the CC to reduce the evaporator thickness to only 8 mm. Simultaneously, a wick was installed inside the liquid line, connecting it directly to the wick inside the evaporator, which could prevent the vapor from entering the liquid line and ensure that the LHP could start up successfully. Liu et al. [22] proposed a composite evaporator with a copper heating surface and a stainless steel shell. At the same time, reinforced ribs were installed inside the evaporator to divide the CC into two parts, thus solving the pressure problem of the evaporator under high heat load on a large heating surface. Additionally, Aono et al. [23] investigated the effect of the condenser diameter of the LHP on the flow pattern inside the condenser tube. The results showed that in the 1/2-in condenser, the vapor was dominated by loop flow, which prevented some of the vapor from entering the CC directly without condensation, resulting in a low thermal resistance of 0.004 °C/W at 6.2 kW. Ling et al. [24] designed an interlaced microchannel condenser with an enlarged heat transfer area, 6.4 times greater than conventional parallel condenser. The preparation and startup times of the interlaced LHPs were 60 s and 140 s, respectively, outperforming parallel LHP.

Secondly, the working fluid is an important factor affecting the performance of LHPs. Maydanik et al. [25] designed cylindrical LHPs, using ammonia as the working fluid. Under air cooling conditions, the maximum heat load reached 110 W, and the measured minimum thermal resistance was 0.53 °C/W. Anand [26] conducted tests on flat-plate LHPs with acetone, methanol, n-pentane, and ethanol. The results indicated that methanol had the highest heat load limit, while n-pentane had the lowest operating temperature. Zhao et al. [27] designed an aluminum alloy LHP for land applications, employing R1233zd(E) as the working fluid due to its low toxicity and environment-friendly properties. At a heat sink temperature of −10 °C, the maximum heat flux of the LHP was 11.43 W/cm$^2$ with the heat source temperature was below 75 °C. Furthermore, nanofluids, conventional fluids with nanoparticles added to enhance thermal conductivity, have been proven to increase the heat transfer performance of LHPs. Wan et al. [28] found that using a 1.0 wt% Cu-water nanofluid reduced the evaporator wall temperature by 12.8 % and thermal resistance by 21.7 % compared to the water LHP at a heat load of 100 W. Salarnia et al. [29] conducted molecular dynamics simulations to investigate the physical and thermal properties behaviors of water and Fe-$Fe_2O_3$-$Fe_3O_4$/water nanofluids in a copper wall oscillating heat pipe (OHP). The simulated numerical values of heat flux of Fe-$Fe_2O_3$-$Fe_3O_4$/water nanofluids in the OHP increased by 1462 W/m$^2$, 1505 W/m$^2$, and 1561 W/m$^2$, respectively. Moreover, Jin et al. [30] explored the influence of magnetic field on the density, temperature, velocity, and heat transfer profiles. The presence of an external magnetic field enhanced the thermal performance of the nanofluid in the OHP, thereby expanding its potential applications in electronic systems.

In addition, the wick design is another important factor in LHP optimization. The performance of LHP heavily relies on the characteristics of the wick. Consequently, the materials, processes and performance optimization of the wick structure have become prominent research topics among scholars. The main materials currently used for the manufacture of wicks include wire mesh [31,32], sintered metal powders [33,34] and metal foams [35,36]. And novel types of wicks have been proposed to further improve the wick performance. Solomon et al. [37] used carbonization to produce a water-insoluble and structurally stable biochar wick, resulting in a 7 °C decrease in evaporator temperature and a significant reduction in total thermal resistance from 0.75 to 0.17 °C/W. Weisenseel et al. [38] adopted biomorphous silicon carbide as a wick material in flat evaporator LHPs. The wick was easy to fabricate and machine without causing pore closure. The LHP successfully started up at a minimum heat load of 50 W and had a thermal resistance of 0.3559 °C/W at a heat load of 200 W. Nakamura et al. [39] chose sub-nanometre porous glass as the primary wick ultra-micro (0.1 μm class) pore diameter, enabling the LHP to operate under 2 m antigravity conditions with a 6.5 m vapor line length and a maximum heat load of 85 W. Cao et al. [40] prepared a $Ti_3(Al,Si)C_2$ wick with double pore size and better hardness. The LHP successfully started up at 30 W and the thermal resistance reached the minimum 0.391 °C/W at 140 W heat load. Li et al. [41] prepared a porous $SI_3N_4$ ceramic wick and investigated the effect of porosity and pore size on capillary and heat transfer properties, demonstrating that the liquid uptake capacity of wicks was dependent on their liquid storage capacity. And the higher open porosity, the stronger the liquid uptake capacity. Esarte et al. [42] used 3D printing technology to manufactured a primary wick with the tailored geometry and pore size, which resulted in an approximately 10 % enhancement in heat transfer rate compared to conventional LHPs using standard wick designs. Xu et al. [43] proposed a double-layer composite copper wick with high evaporation efficiency and high permeability to eliminate the heat leakage from the system at high heat loads. This optimization led to rapid startup, achieve a 140 W maximum heat load. He et al. [44] proposed a pouring porous wick method, characterized by simplicity, low production cost and high yield of prepared samples. The pour size could be customizable according to evaporator dimensions, and the LHPs equipped with such wicks successfully operated within a heat load range of 5 W to 80 W. Zhang et al. [45] used polyacrylonitrile carbon fibers as raw materials and employed the arc spraying method to fabricate metal–carbon fiber composite wicks. The LHP using methanol demonstrated optimal performance, maintaining a heat source temperature of 84.47 °C under a heat load of 120 W. Kumar et al. [46] oxidized a copper wick to reduce heat leakage, with the oxidized copper wick leaking around 7 % of input heat loads compared to 18 % for the pure wick. Phan et al. [47,48] prepared a hydrophilic PTFE wick, the LHP handled 1000 W heat load and achieved a minimal thermal resistance of 0.052 °C/W.

In summary, many researches focused on developing new high-performance wicks by proposing novel materials. In addition to the choice of materials, the surface structure and wettability also play a significant role in vapor nucleation [49], which is important for improving the heat transfer performance of the LHP. Ahn et al. [50] found that surface wettability could increase the critical heat flux density, while the micro- and nanostructures surface treatments enhanced the spreading of the liquid on the surface, further improving the heat transfer capacity. Dong et al. [51] investigated the influence of microstructures on vapor nucleation and vapor ejection. Compared to smooth surface, microstructured surface had the potential to increase the evaporation site density, promote vapor nucleation, and consequently enhance the heat flux. Guo et al. [52] achieved super-hydrophilic sintered wicks by treating the wick surface with $H_2O_2$. Nam et al. [53] obtained controllable wettability on copper surfaces through oxidation methods, which enhanced capillarity and resulted in an improvement of

70 % in the critical heat flux.

In this study, a hydrothermal carbonization method was employed to carry out surface treatment on a nickel powder sintered biporous wick, creating a carbon spheres modified nickel wick (CSs-Ni-Wick). The CSs-Ni-Wick offers several advantages, including large pores for reducing flow resistance and enlarging the evaporation surface, small pores for enhancing capillarity, and a higher concentration of hydrophilic functional groups on its surface to accelerate fluid infiltration. Subsequently, a flat plate evaporator LHP with CSs-Ni-Wick was designed, and its heat transfer performance was tested and investigated. The results demonstrated that the LHP with CSs-Ni-Wick operated smoothly at low heat loads and achieved a maximum heat load of 140 W (20 W/cm$^2$) at a heat source temperature of not exceeding 85 °C and a heat sink temperature of 0 °C.

## 2. Experimental methods

### 2.1. Materials

T255 carbonyl nickel powder was produced by the Canadian company INCO. Sodium carbonate (≥99.8 %, AR), glucose (≥99.5 %, AR), ethanol (≥99.7 %, AR) and methanol (≥99.5 %, AR) were purchased from Sinopharm Chemical Reagent Co., Ltd. All above reagents were used as received. Ultrapure water was purchased from Hangzhou Wahaha Group Co., Ltd.

### 2.2. Preparation of CSs-Ni-Wick

According to the method described in the literature [54], the biporous wick was prepared by using T255 carbonyl nickel powder with a particle size of 2.2–2.8 μm and a loose packing density of 0.520–0.65 g/cm$^3$. Sodium carbonate powder with a particle size of 48–75 μm was used as the pore-forming agent. As shown in the Fig. 1, the nickel powder with volume ratio of 30 % and sodium carbonate powder with volume ratio of 70 % were mixed to achieve a uniform mixing. The mixture was filled into a mold and kept under a pressure of 5 MPa for 10 min before being demolded, resulting in a compacted wick embryo consisting of mixed nickel powder and sodium carbonate. The wick embryo was placed in a vacuum sintering furnace, where the nickel powder melted and shrank at an appropriate sintering temperature of 700 °C, forming small pores. After sintering, the wick embryo was rinsed with pure water, and only the sodium carbonate powder was dissolved in pure water, resulting the initial pH level of the solution was alkaline. By performing multiple rinses on the wick embryo using pure water until the pH of the solution reached neutrality, the sodium carbonate powder was completely dissolved, leading to the formation of large pores. The rinsed wick was then rapidly dried in a drying oven, resulting in the biporous wick.

In order to improve the hydrophilicity of the biporous wick, the study adopted the glucose hydrothermal carbonization method from reference [55]. First, a glucose solution was prepared at a concentration of 0.08 g/ml. Next, this solution, along with the biporous wick, was introduced into a hydrothermal reactor. The temperature within the reactor was raised to 180 °C and consistently maintained for 4 h to facilitate the carbonization process. Upon completion of the heating cycle, the reactor was permitted to cool naturally. Subsequently, the wick was removed and washed repeatedly with pure water and ethanol solution, continuing until the clarity of the rinsing solvents indicated the absence of any residual contaminants. Finally, the cleaned wick was dried to yield the "CSs-Ni-Wick". The manufacturing process is illustrated in Fig. 1.

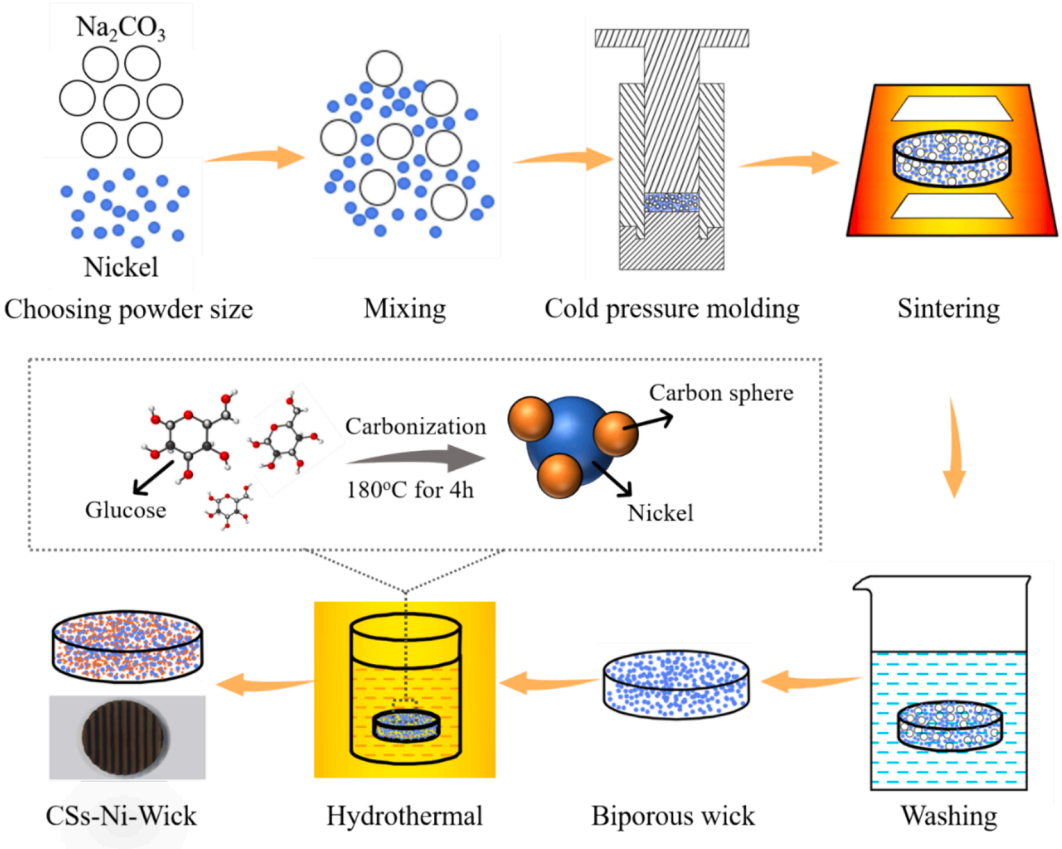


**Fig. 1.** Schematic of the hydrothermal treatment process for the CSs-Ni-Wick.

### 2.3. Design of the LHP with flat evaporator

The performance of the wick is closely related to the heat transfer capability of the LHP. The performance of the wick can be studied by constructing an LHP testing system. As shown in the Fig. 2(a), the LHP mainly consists of an evaporator, vapor line, condenser, liquid line, and charging port.

The Fig. 3(a) shows the explosion photo of the evaporator of the LHP, consisting of heating surface, CSs-Ni-Wick and evaporator shell. Fig. 3 (b) shows the structure of the evaporator. The configuration of the CSs-Ni-Wick is shown in Fig. 3(c) and (d). The ribbed side of the CSs-Ni-Wick fits tightly with the heating surface to form a vapor chamber, and the other side forms a CC with the shell. After applying heat load, the porous structure of the wick produces vapor core. The working fluid absorbs most of the heat and undergoes a phase change to vapor. It then travels through the vapor line to reach the condenser for condensation. At the same time, the wick provides capillarity to supply liquid working fluid to the vapor core, ensuring the continuous and stable operation of the LHP. In addition, another portion of the heat source is conducted through the evaporator shell and wick to the CC, where it is absorbed by the sensible heat of subcooled fluid flowing out of the condenser. The overall material of the LHP is brass, methanol is used as the working fluid for system compatibility, and the loop is internally evacuated to $3.0 \times 10^{-4}$ Pa before charging the working fluid. The LHP was placed horizontally and the charge ratio was vol. 72 %. Table 1 shows the detailed parameters of the LHP components.

Fig. 2(b) shows a schematic diagram of the arrangement of the thermocouples throughout the system. The accuracy of the thermocouples is ±0.5 °C. The temperature data is collected by the Keithley 2700 data acquisition system. Thermocouples T1-T4 record the temperature of the evaporator outlet, the condenser inlet, the condenser outlet and the evaporator inlet, respectively. Thermocouples T5-T8 record the temperature of the heat source. Thermocouple T9 and T10 record the temperature of the CC wall the ambient temperature, respectively. The heat source consists of three heating rods coupled to cylindrical copper blocks. The heat output is recorded by a wattmeter with an accuracy of 0.5 %. To reduce the thermal contact resistance between the evaporator and the heat source, a uniform layer of thermal grease is applied to the contact surface. The heat source and pipes are wrapped with insulating cotton to minimize heat loss to the environment.

## 3. Experimental results and discussions

### 3.1. Morphology and structure analysis on CSs-Ni-Wick

The morphology and microstructure of the samples were observed using a field emission scanning electron microscope (FSEM, Nova NanoSEM 450, FEI, NED). Thermogravimetric analysis was conducted on a thermalgravimetric analyzer (TGA 8000, PerkinElmer, USA). Raman scattering was performed on a Raman spectrometer (LabRAM HR800, Horiba Jobin Yvon, FR). Surface functional groups were measured by Fourier transform infrared spectroscopy (FTIR, Nicolet iS50R, Thermo Scientific, USA). Contact angles were measured by drop shape analyzer (DSA30, KRUSS, DE).

Fig. 4(a) shows the SEM image of the biporous wick surface before hydrothermal treatment, where the surface is relatively uniformly distributed with large and small pores. Fig. 4(b) shows an SEM image of the CSs-Ni-Wick surface after hydrothermal treatment. Both large and small pores are preserved, while a multitude of spherical carbon spheres have directly grown on the nickel substrate. As shown in Fig. 4(c), the particle size of these carbon spheres is measured approximately 1000–2000 nm.

To further investigate the properties of the surface-modified wick, the thermal stability of both biporous wick and CSs-Ni-Wick was characterized by thermogravimetric analysis. As shown in Fig. 5, the heating rate temperature simulates the temperature variation and running time of the LHP in continuous operation at elevated heat loads. It can be seen that there is no mass loss for either biporous wick or CSs-Ni-Wick at 85 °C. To enable the wick to operate at even higher temperatures, the mass of both remains constant even at the temperature of 200 °C. This result fully demonstrates that CSs-Ni-Wick has good thermal stability, and the carbon spheres will not decompose at high temperatures within 200 °C, which is promising for application.

Raman spectroscopy was employed to compare the molecular structures of the wicks before and after hydrothermal treatment, as shown in Fig. 6(a). Raman spectra show the vibrational modes of the wick, providing information about its molecular structure and bonding characteristics. Spectral peaks may emerge corresponding to specific functional groups or carbonaceous materials, indicating changes in the chemical composition of the wick after the hydrothermal carbonization treatment. The Raman peak observed at 1585 $cm^{-1}$ in the spectrum belongs to the G-peak of the carbon-based material [56], showing that the post-hydrothermal treatment wick contains carbon, which remains stable even after high-temperature thermogravimetric testing.

FTIR spectroscopy provides information about molecular vibrations and chemical bonds within the wick. The technique can be employed to

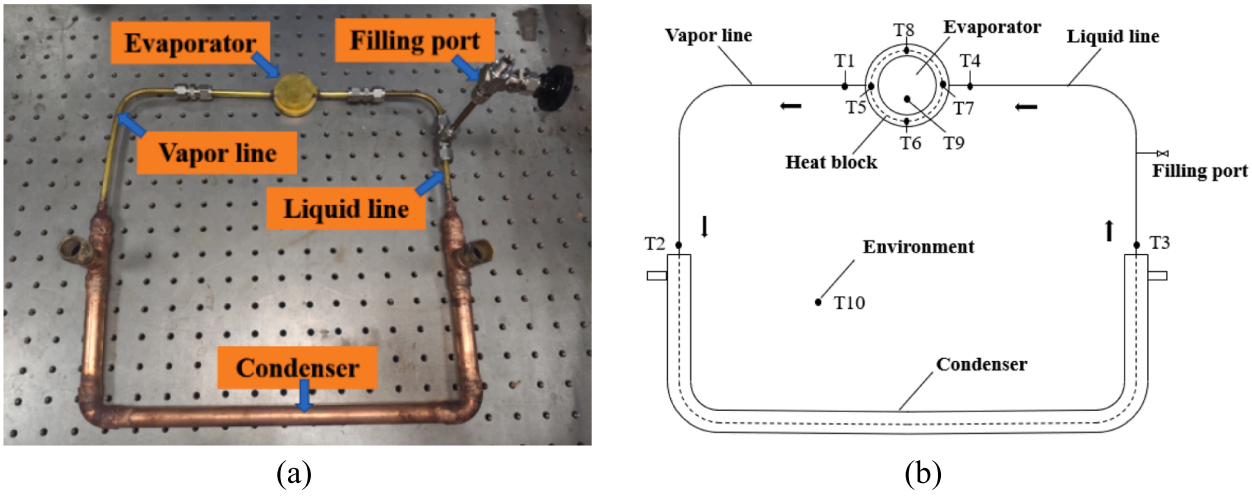


**Fig. 2.** Diagram of the LHP(a) and the arrangement of thermocouples(b).

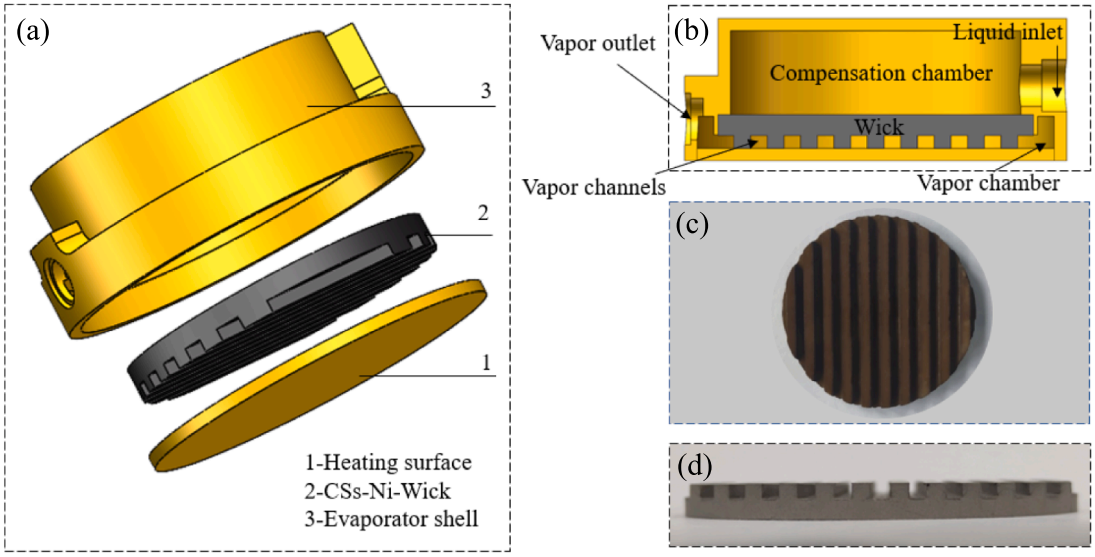


**Fig. 3.** Design of the evaporator(a)(b) and configuration of the CSs-Ni-Wick. (c) Front view. (d) Lateral view.

**Table 1**
Main structure parameters of the LHP components.

| | | |
|---|---|---|
| Evaporator | Heating diameter/mm | 42.78 |
| | Height/mm | 16.9 |
| CC | Inner diameter/mm | 34.78 |
| | Height/mm | 10.02 |
| CSs-Ni-Wick | Porosity | 72.6 % |
| | Diameter × thickness/mm | 37.78 × 4.02 |
| Vapor line | Diameter I/O × Length/mm | 4/6 × 270 |
| Liquid line | Diameter I/O × Length/mm | 4/6 × 235 |
| Condenser | Inner tube diameter I/O/mm | 4/6 |
| | Out tube diameter I/O/mm | 12/16 |
| | Length/mm | 685 |

reveal changes in surface functional groups and chemical composition induced by the hydrothermal treatment. Therefore, further FTIR analysis was conducted on the biporous wick and CSs-Ni-Wick after thermogravimetric drying. Fig. 6(b) shows the present of two resonance absorption peaks associated with oxygen-containing functional groups, i.e. —OH and C═O, at 1626 $cm^{-1}$. This indicates that the CSs-Ni-Wick surface contains a large number of oxygen-containing functional groups. Meanwhile, the C═C resonance peaks were detected at 1626 $cm^{-1}$ and the $CH_2$ resonance peaks were observed at 2825 $cm^{-1}$ and 2922 $cm^{-1}$, indicating the presence of graphite structure on the CSs-Ni-Wick surface. The peak observed at 3443 $cm^{-1}$ is due to OH bonds (hydroxyl and carboxyl groups) and absorbed water [57,58]. Comparison indicates that the intensity at 3443 $cm^{-1}$ for CSs-Ni-Wick is significantly higher than that of the biporous wick, suggesting an increase in oxygen-containing functional groups on the CSs-Ni-Wick surface after the hydrothermal process.

Fig. 7 shows the contact angle of water on the wicks, measured using the captive bubble method. Firstly, the wick was immersed in the liquid phase, allowing a bubble to form and be captured on the underside surface of the wick for contact angle measurement and characterization. Thereafter, the contact angle of water on the wick surface was calculated using Laplace-Young equation fitting method. It can be seen that the contact angles of water on the biporous wick and the CSs-Ni-Wick surfaces are 67.5° and 25.8°, respectively, indicating that the affinity of the CSs-Ni-Wick surface for water has been increased.

Fig. 8 shows a schematic of the solid–liquid interface of the wick. Methanol is a polar solvent as working fluid and the oxygen-containing functional groups of CSs-Ni-Wick can form hydrogen bonds with methanol molecules, increasing the affinity of the wick surface for methanol, reducing the contact angle, and improving the penetration

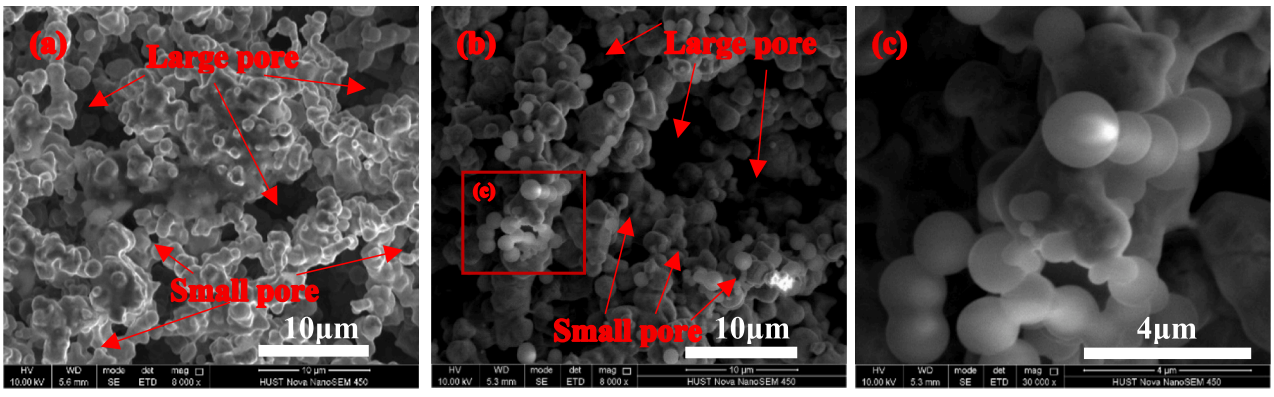


**Fig. 4.** The SEM image of the microporous structure: (a) for biporous wick(×8000); (b) for CSs-Ni-Wick(×8000); (c) for CSs-Ni-Wick(×30000).

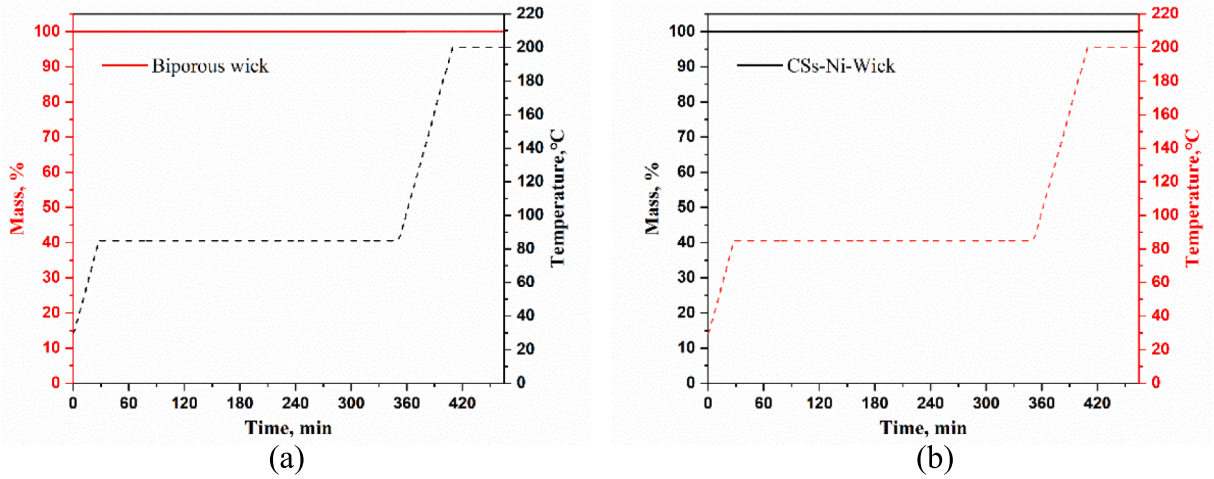


**Fig. 5.** TGA graph, weight loss against temperature:(a) for biporous wick, (b) for CSs-Ni-Wick.

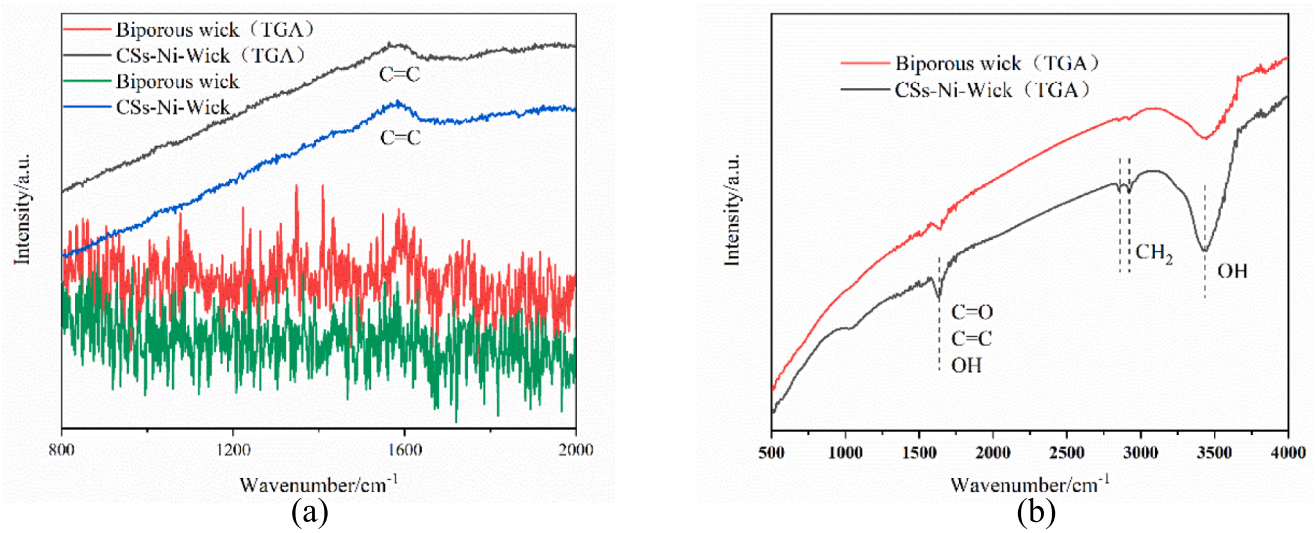


**Fig. 6.** The Raman(a) and FTIR(b) spectra of the biporous wick and CSs-Ni-Wick.

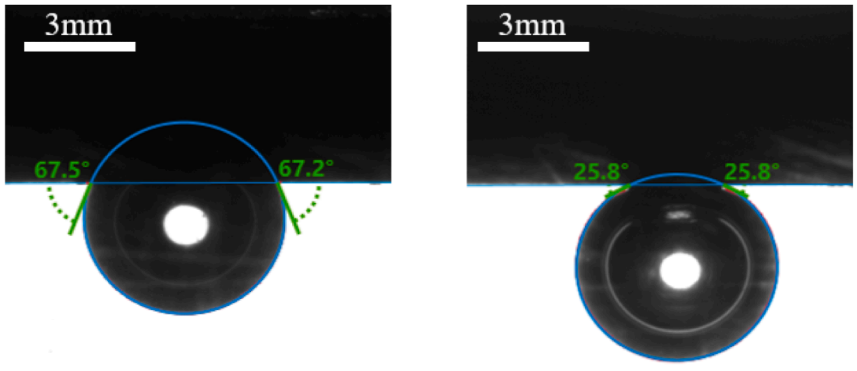


**Fig. 7.** Captive bubble method for measuring the contact angle of water on the biporous wick(a) and CSs-Ni-Wick(b).

effect of the working fluid into the wick, thus enhancing the capillarity.

### 3.2. Start-up performance

The LHP with CSs-Ni-wick was placed horizontally to test its start-up performance under different heat loads, successfully operating in the range of 15 W-140 W while keeping the required heat source temperature below 85 °C. Fig. 9 gives the start-up processes at heat load of 20 W. Compared to typical negative pressure LHP [59], the LHP with CSs-Ni-wick did not exhibit temperature overshoot at low heat load

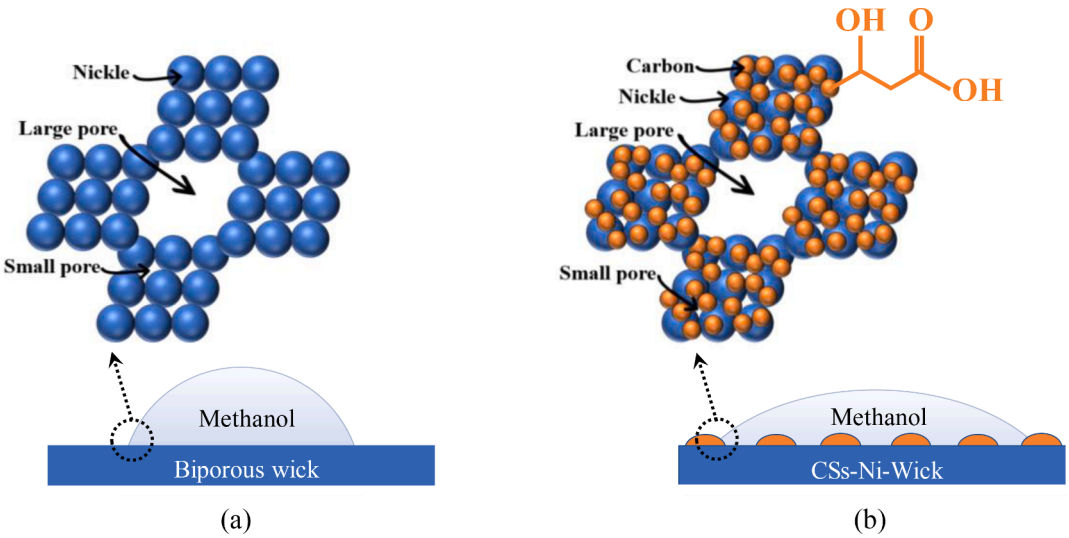


**Fig. 8.** Schematic of the solid–liquid interface of the biporous wick(a) and CSs-Ni-Wick(b).

conditions. Moreover, no significant temperature oscillations were detected among the different measuring points in the system. When the heat sink temperature was lower than the ambient temperature, there was a small increase in the condenser inlet temperature and a small decrease in the condenser outlet temperature, as shown in Fig. 9(a) and (b), which indicated that the vapor generated after the application of a heat load did not accumulate for a long time in the vapor chamber but rather flowed into the condenser through the vapor line at a low flow rate. The presence of the carbon spheres provided a larger surface area for vaporization to occur. The increased surface area accommodated a great number of vaporization cores, effectively increasing the density of vaporization cores. Meanwhile, the microstructure of the carbon spheres

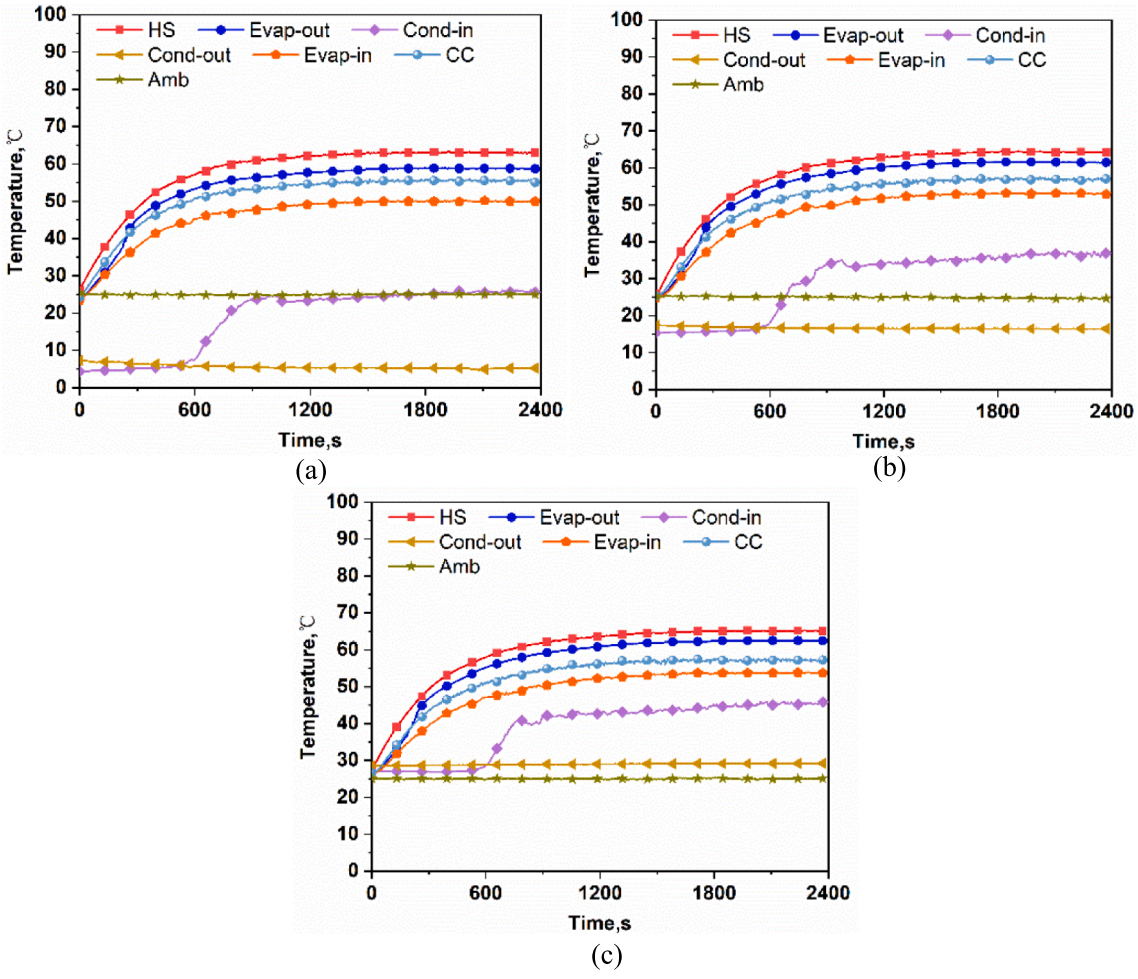


**Fig. 9.** Start-up processes on Q = 20 W at the different heat sink temperature: (a) for 0 °C; (b)for 15 °C; (c)for 30 °C.

promoted the formation of small-scale capillary channels. These capillary channels facilitated the rapid flow of vapor, enabling the vapor to escape more quickly from the wick surface and accelerating the circulation rate. Consequently, the heat leakage effect to the CC was reduced due to the quicker return rate of the subcooled working fluid to the CC. This resulted in the establishment of a more stable driving force on both sides of the wick, enabling the LHP to operate stably at low loads. When the heat sink temperature was higher than the ambient temperature, as depicted in Fig. 9(c), the change in temperature at the condenser inlet and outlet was not obvious following the application of the heat load, and the LHP continued to start up smoothly.

The start-up performances were tested under higher heat load conditions with the same heat sink temperature of 0 °C. Fig. 10(a) shows the start-up performance of the LHP at a heat load of 70 W. As the heat load increased, the rate of vapor generation speeded up, allowing the LHP to quickly start up and achieve stability. Fig. 10(b) shows the start-up performance of the LHP at the maximum heat load of 140 W (20 W/cm$^2$), while the heat source temperature reaching the maximum of 85 °C. Despite these heightened heat loads and temperatures, the LHP successfully starts up and operates stably, demonstrating its high heat dissipation capacity.

### 3.3. Operation under variable heat load cycle

The performance of the LHP under a variable heat load cycle is indicative of its thermal capability and thermal stability. Therefore, in order to further investigate the performance of the LHP under a variable heat load cycle, the LHP was subjected to a series of tests at different heat sink temperatures of 0 °C, 15 °C and 30 °C. The LHP was able to start up smoothly even at a low heat load of 15 W. At the same time, the LHP demonstrated a rapid response to changes in heat load and stabilized the temperature of the heat source.

Fig. 11 shows that the operational characteristics and stability of the LHP as the heat load is gradually increased at a heat sink temperature of 0 °C. The sequence started with the application of a 15 W heat load to allow the system to reach a stable state. The heat load was then increased to 20 W, followed by increased steps of 10 W each time, all the way up to a maximum of 140 W. At a heat load of 15 W, the condenser inlet temperature was mainly influenced by the vapor on the tube walls and the heat conduction of the cooling water through the tube walls within the condenser. When evaporation rate was lower than the condensation rate, the vapor cooled rapidly as it entered the condenser. As a result, the condenser inlet temperature initially increased and then decreased. At a heat load ranging from 30 W to 40 W, the instability of the evaporation rate leaded to the fluctuations in the vapor–liquid

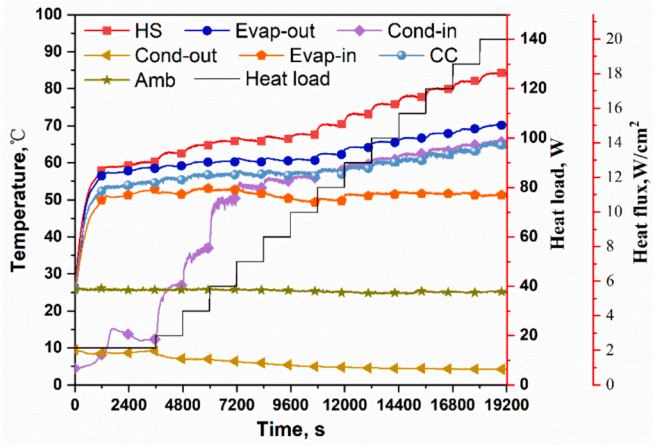


**Fig. 11.** Continuous operation with a stepwise heat load cycle at 0 °C.

interface, resulting in small temperature fluctuations at the condenser inlet. Continuing to increase the heat load, the evaporation rate increased, generating more vapor and propelling the vapor–liquid interface further into the condenser. Consequently, the temperature at the condenser inlet reached a steady state. However, the temperature fluctuations in the condenser inlet did not result in fluctuations in the other parts of the system. This was mainly due to the excellent performance of CSs-Ni-Wick, which enhanced the wettability of the working fluid with the wick and increased the density of the vapor core, facilitating faster vapor generation that promptly enters the condense. At the same time, the combined effect of the capillary force and the phase change driving force resulted in the rapid flow of liquid from the condenser back to the CC. This established a positive circulation of the working fluid within the system, achieving stable operation of the LHP.

Figs. 12 and 13 illustrate the test results conducted on the LHP with a continuously increasing heat load under heat sink temperatures of 15 °C and 30 °C, respectively. Similarly, as the heat sink temperature increased, the condenser inlet temperature experienced persistent fluctuations at low heat loads, whereas the other temperature sensors remained stable. As the heat sink temperature increased, the maximum heat load that the LHP was able to withstand decreased.

### 3.4. Analysis of thermal performance

Fig. 14 shows the relation between the LHP operating temperature during steady state operation and the corresponding heat load. The

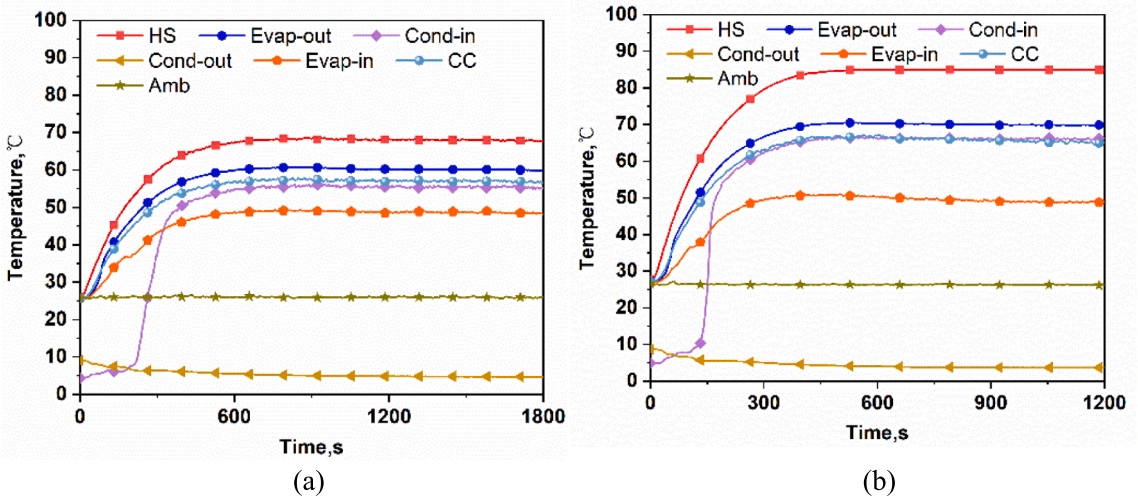


**Fig. 10.** Set-up processes at a heat sink temperature of 0 °C: (a) Q = 70 W; (b) Q = 140 W.

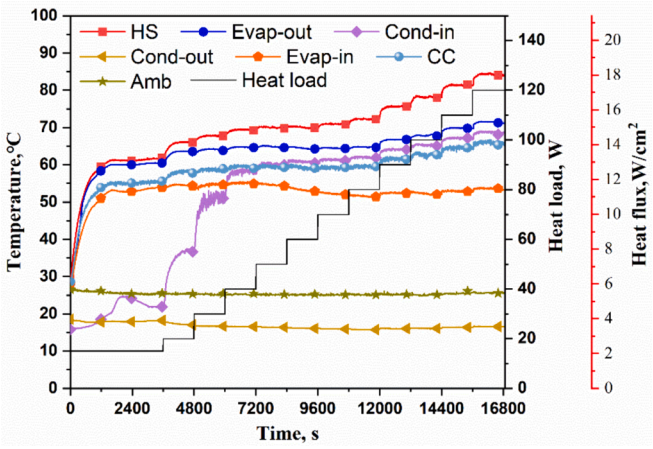


**Fig. 12.** Continuous operation with a stepwise heat load cycle at 15 °C.

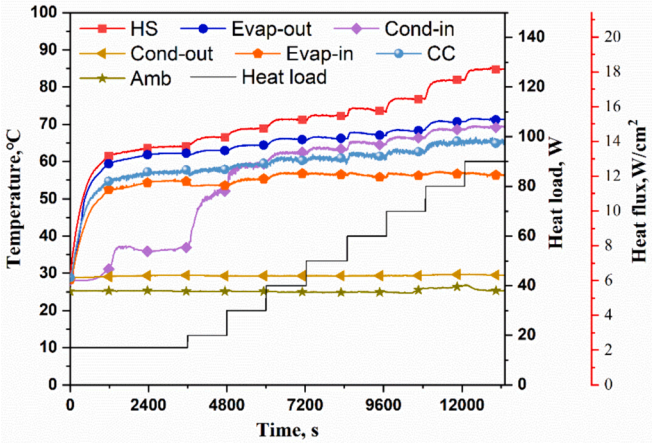


**Fig. 13.** Continuous operation with a stepwise heat load cycle at 30°C.

operating mode of the LHP is generally divided into variable conductance mode and fixed conductance mode. Before the heat load reached 70 W, it operated in the variable conductance mode. At low heat loads, the flow velocity of the vapor and liquid within the pipe was low, and the temperatures were affected by factors such as the ambient temperature, heat conduction through the pipe walls, and the flow of the working fluid within the pipe. As the heat load increased, the vapor–liquid interface was in the vapor channel and extended into the wick. With a rapid rise in the interface, the phase change process accelerated, leading to an increase in the rate of evaporation. Consequently, the circulation speed of the working fluid in the LHP accelerated. This resulted in an increase in the condenser inlet temperature and a decrease in the condenser outlet temperature, indicating that the working fluid had been sufficiently subcooled to carry away any heat leaked from the CC. The temperature of the CC did not change significantly as the thermal load increased, and the temperature of the heat source could be effectively controlled to remain below 70℃.

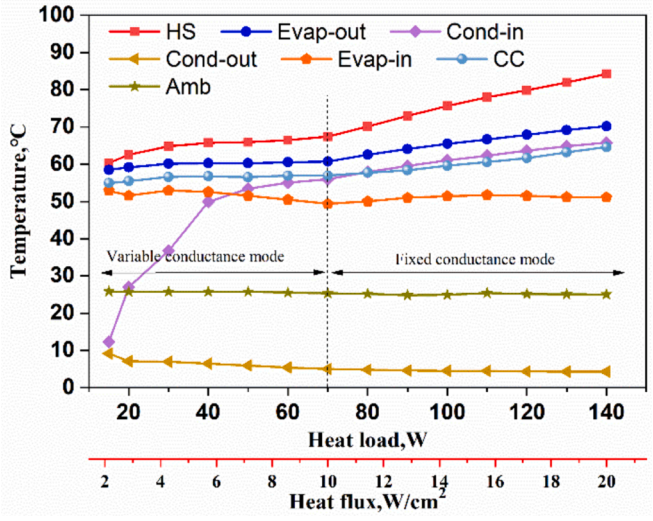


**Fig. 14.** Characteristic point temperatures of the LHP at 0 °C.

After a heat load of 70 W, the LHP is in constant thermal conductivity mode. When the heat load increased, the vapor–liquid interface inside the wick migrated towards the CC. This resulted in an increased thickness of the superheated vapor layer between the vapor–liquid interface and the heating surface, which elongated the heat transfer path and increased the contact thermal resistance. Simultaneously, the heat leak through the wick increased, leading to a rise in the temperature of both the CC and the heat source. In constant thermal conductivity mode, the temperature of the LHP exhibited a linear increase as the thermal load increased.

The LHP serves as a heat dissipation component, and its heat transfer capability can be characterized by calculating the thermal resistance of the LHP, the evaporator and the condenser, which are as follows [60]:

$$R_{LHP} = \frac{T_{HS} - T_{Cond}}{Q} \tag{1}$$

$$T_{Cond} = \frac{T_{Cond-in} + T_{Cond-out}}{2} \tag{2}$$

$$R_{Evap} = \frac{T_{HS} - T_{Evap-out}}{Q} \tag{3}$$

$$R_{Cond} = \frac{T_{Cond} - T_{Heatsink}}{Q} \tag{4}$$

where $T_{HS}$ is the temperature of heat source, $T_{Cond}$ is the average temperature of the temperature of $T_{Cond\text{-}in}$ and $T_{Cond\text{-}out}$, $T_{Evap\text{-}out}$ is the temperature of the evaporator outlet, $T_{Heat\ sink}$ is the temperature of heat sink and $Q$ is the heat load.

The uncertainly of $R_{LHP}$ can be calculated by [61]

$$\frac{\delta R_{LHP}}{R_{LHP}} = \sqrt{\left(\frac{\delta t}{t}\right)^2 + \left(\frac{\delta Q}{Q}\right)^2} \tag{5}$$

$$\delta t = \sqrt{\sum_{i=1}^{4}\left(\frac{1}{4}\delta T_{HS,i}\right)^2 + \sum_{i=1}^{2}\left(\frac{1}{2}\delta T_{Cond,i}\right)^2} \tag{6}$$

$$\delta t = \sqrt{\frac{1}{4}\sum_{i=1}^{4}\left(\delta T_{HS,i}\right)^2 + \frac{1}{2}\sum_{i=1}^{2}\left(\delta T_{Cond,i}\right)^2} \tag{7}$$

$$t = T_{HS} - T_{Cond} \tag{8}$$

where $T_{HS,i}$ is the temperature of heat source measured by fore thermocouples and $T_{Cond,I}$ is the temperature of $T_{Cond\text{-}in}$ and $T_{Cond\text{-}out}$.

Fig. 15 shows the variation of the thermal resistance of the evaporator, condenser and the LHP at different heat sink temperatures and heat loads. The thermal resistance of the LHP is primarily influenced by the thermal resistances of the evaporator and condenser. The thermal resistance of the evaporator is associated with the expansion process of the vapor–liquid interface. When the heat load increased, the vapor–liquid interface in the evaporator expanded into the wick, which leaded to a faster phase change process and a decrease in the thermal resistance of the evaporator. Additionally, more vapor flowed to the condenser, improving the cooling efficiency and reducing the thermal resistance of the condenser. Consequently, the thermal resistance of the LHP

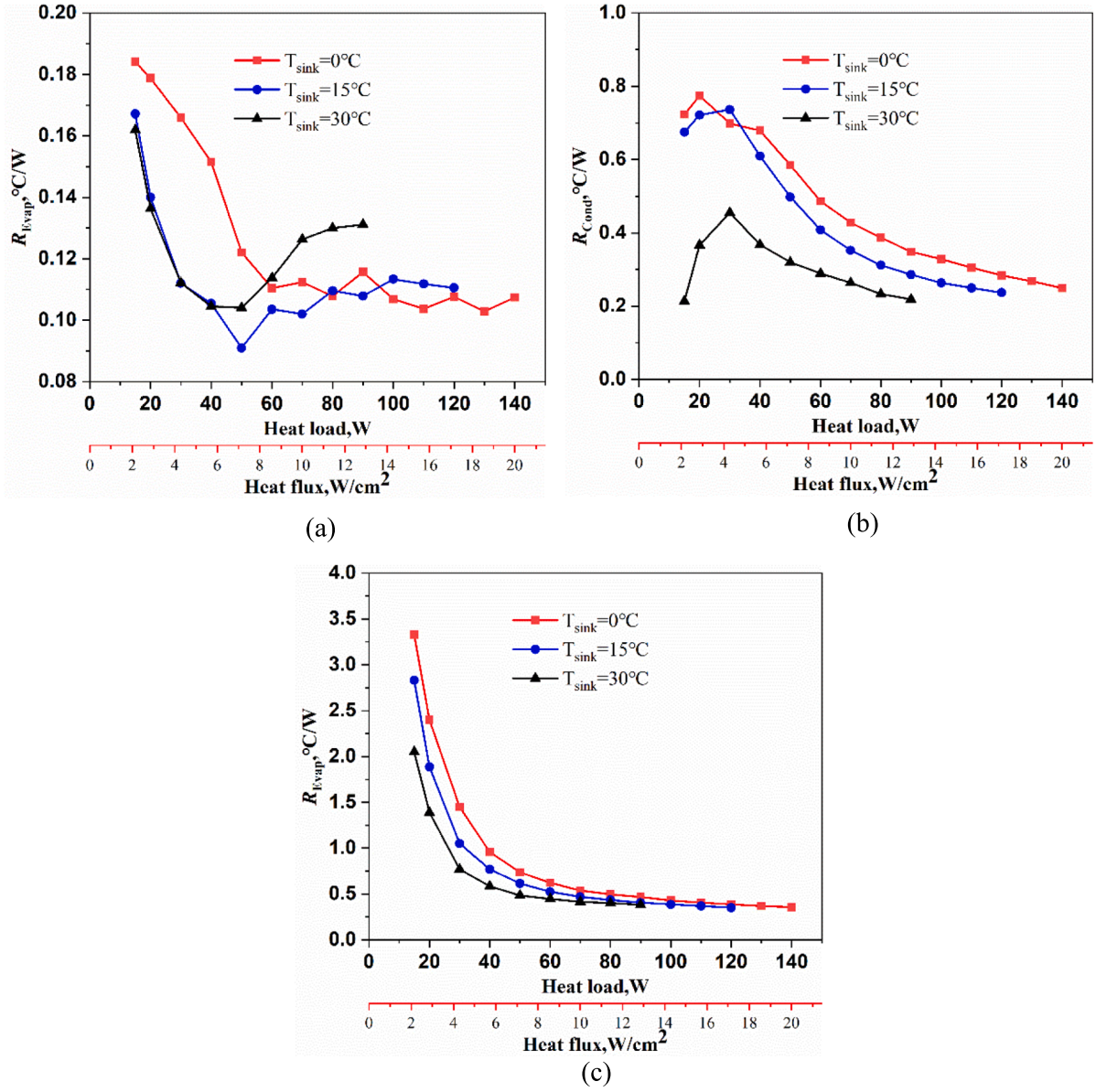


**Fig. 15.** Thermal resistance at three heat sink temperatures: (a) thermal resistances of the evaporator; (b) thermal resistances of the condenser; (c) thermal resistances of the LHP.

decreased as the heat load increased. When the vapor–liquid interface in the evaporator reached its maximum expansion and the condensation efficiency of the condenser reached its limit, the thermal resistance of the LHP gradually stabilized. The minimum thermal resistance of the LHP was 0.357 °C/W at a heat load of 140 W. It's important to note that as the heat sink temperature increases, the temperature difference between the evaporator and the heat sink decreases, resulting in a decrease in the thermal resistance of the LHP under the same heat load.

Through error analysis of measuring instrument accuracies, the maximum uncertainty of the LHP thermal resistance was ±1.26 % at a heat load of 10 W and the minimum uncertainty was ±0.51 % at a heat load of 140 W.

### 3.5. Data comparison

Appendix A listed the working fluid, heat load, heat flux, the stable temperature at the heating surface and the heat sink temperature in this study and other studies [16,37,62–64]. Fig. 16 shows the stable temperature of the heating source corresponding to different heat fluxes. Compared with the LHPs in other studies, the LHP with CSs-Ni-Wick is capable to operate over a wider range of heat fluxes while maintaining lower heat source temperature. Among them, Liu et al. [64] designed a flat type LHP with a biporous wick, in which the evaporator was made of brass and the working fluid was methanol. In the horizontal position, the LHP was able to dissipate a heat flux of 16.8 W/cm$^2$ with a temperature of the evaporator wall below 85℃, and the minimum LHP thermal resistance was 0.46 °C/W. When the temperature of the evaporator wall is below 85 °C, the LHP with CSs-Ni-Wick has a 19 % improvement in maximum heat flux compared to the LHP with biporous wick, and a 22 % reduction in the minimum LHP thermal resistance. This comparison verifies that the CSs-Ni-Wick can significantly improve LHP operational performance.

## 4. Conclusions

This paper introduced the application of CSs-Ni-Wick in LHP. Firstly, the manufacture process of the CSs-Wick was described and its structure and thermal properties were characterized. The performance of the CSs-

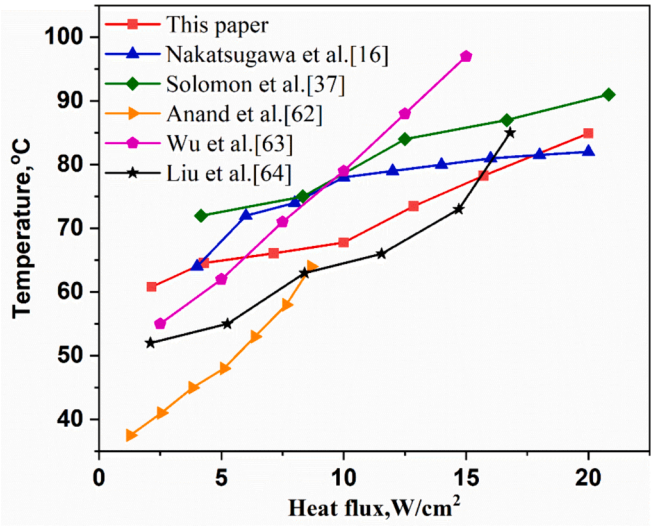


**Fig. 16.** Comparison of stable temperatures with other studies [16,37,62–64].

Wick was investigated by testing the LHP with CSs-Ni-Wick. The main conclusions were summarized as follows.

(1) A hydrothermal method was used to modify the surface of a conventional sintered nickel powder wick, resulting in the deposition of carbon spheres on the surface. The contact angles of water on the biporous wick and CSs-Ni-Wick were 67.5° and 25.8°, respectively. Raman spectroscopy and FTIR revealed that the CSs-Ni-Wick contains a higher concentration of hydrophilic functional groups, which increased the hydrophilicity of the wick and may be useful for researchers and developers of heat exchange technology.
(2) In the horizontal position, the LHP with CSs-Ni-Wick was able to start up smoothly at heat load as low as 15 W without temperature overshoot. Furthermore, the LHP was able to operate stably, effectively suppressing the generation of temperature fluctuations. The LHP with CSs-Ni-Wick exhibited good thermal responsiveness at different heat sink temperatures.
(3) The maximum heat load was 140 W (20 W/cm$^2$) when the heat source temperature was required to be not more than 85℃ and the minimum LHP thermal resistance was 0.357 °C/W. The LHP with CSs-Ni-Wick has a 19 % improvement in maximum heat flux compared to LHP with biporous wick, and a 22 % reduction in the minimum LHP thermal resistance.

There are several areas that need to be improved and further investigated in future studies. It is necessary to test different working fluids with the CSs-Ni-Wick to ascertain the suitability, compatibility and service life. A visualization test platform should be used to investigate the permeability and heat transfer performance of the CSs-Ni-Wick. Furthermore, numerical simulations should be conducted to investigate the relationship between the wick structure and the heat transfer performance.

## Declaration of competing interest

The authors declare that they have no known competing financial interests or personal relationships that could have appeared to influence the work reported in this paper.

## Data availability

Data will be made available on request.

## Acknowledgement

This work is supported by the National Natural Science Foundation of China (Grant No. 52076088), and the National Key Research and Development Program of China (Grant No. 2022YFB4003801).

## Appendix A. Supplementary data

Supplementary data to this article can be found online at https://doi.org/10.1016/j.applthermaleng.2024.123956.

## References

[1] H. Hu, C. Chen, C. Li, M. Pan, Experimental investigation of roll bond liquid cooling plates for server chip heat dissipation, Appl. Therm. Eng. 226 (2023) 120284.
[2] Y.F. Maydanik, Loop heat pipes, Appl. Therm. Eng. 25 (2005) 635–657.
[3] M.A. Chernysheva, S.V. Vershinin, Y.F. Maydanik, Development and investigation of a loop heat pipe at a high concentration of heat load, Int. J. Heat Mass Transf. 197 (2022) 123316.
[4] N. Watanabe, T. Mizutani, H. Nagano, High-performance energy-saving miniature loop heat pipe for cooling compact power semiconductors, Energ. Conver. Manage. 236 (2021) 114081.
[5] J. Lee, D. Kim, J. Mun, S. Kim, Heat-transfer characteristics of a cryogenic loop heat pipe for space applications, Energies 13 (2020) 1616.
[6] T.D. Swanson, G.C. Birur, NASA thermal control technologies for robotic spacecraft, Appl. Therm. Eng. 23 (2003) 1055–1065.
[7] S. Becker, S. Vershinin, V. Sartre, E. Laurien, J. Bonjour, Y.F. Maydanik, Steady state operation of a copper–water LHP with a flat-oval evaporator, Appl. Therm. Eng. 31 (2011) 686–695.
[8] N. Putra, B. Ariantara, R.A. Pamungkas, Experimental investigation on performance of lithium-ion battery thermal management system using flat plate loop heat pipe for electric vehicle application, Appl. Therm. Eng. 99 (2016) 784–789.
[9] M. Bernagozzi, A. Georgoulas, N. Miché, M. Marengo, Heat pipes in battery thermal management systems for electric vehicles: a critical review, Appl. Therm. Eng. 219 (2023) 119495.
[10] Z. Xu, J. Lu, S. Xing, Thermal performance of greenhouse heating with loop heat pipe solar collector and ground source heat pump, Results Eng. 15 (2022) 100626.
[11] P.V. Chilbule, L.P. Dhole, Heat pipe integrated solar thermal systems and applications: a review, Mater. Today:. Proc. 60 (2022) 1491–1496.
[12] L. Vasiliev, D. Lossouarn, C. Romestant, A. Alexandre, Y. Bertin, Y. Piatsiushyk, V. Romanenkov, Loop heat pipe for cooling of high-power electronic components, Int. J. Heat Mass Transf. 52 (2009) 301–308.
[13] K.G. Domiciano, L. Krambeck, J.P.F. Mera, M.B.H. Mantelli, Study of a new thin flat loop heat pipe for electronics, Heat Mass Transf. 59 (2023) 2035–2056.
[14] X. Zhang, Y. Liu, X. Wen, C. Li, X. Hu, Low-grade waste heat driven desalination with an open loop heat pipe, Energy 163 (2018) 221–228.
[15] X. Zhang, H. Wang, H. Jiang, C. Li, X. Hu, Open loop heat pipes for high-efficiency desalination plant, Appl. Therm. Eng. 193 (2021) 117027.
[16] Y. Nakatsugawa, K. Odagiri, A. Ueno, H. Nagano, Relation between triple phase contact line and vapor groove width for enhancing thermal performance of a loop heat pipe evaporator, Int. J. Heat Mass Transf. 195 (2022) 123139.
[17] Z. Yang, Y. Zhang, L. Bai, H. Zhang, G. Lin, Experimental study on the thermal performance of an ammonia loop heat pipe using a rectangular evaporator with longitudinal replenishment, Appl. Therm. Eng. 207 (2022) 118199.
[18] K. Xiong, L. Meng, S. Wang, L.W. Zhang, Experimental investigation on thermal characteristics of a novel loop heat pipe for cooling high heat flux electronic chips, Int. J. Heat Mass Transf. 187 (2022) 122569.
[19] K. Fukushima, H. Nagano, New evaporator structure for micro loop heat pipes, Int. J. Heat Mass Transf. 106 (2017) 1327–1334.
[20] C. Han, L. He, Z. Tian, B. Xu, Z. Chen, Study of heat dissipation characteristics of loop heat pipe with heat sink of composite material, Appl. Therm. Eng. 200 (2022) 117572.
[21] S. Du, Q. Zhang, P. Hou, C. Yue, S. Zou, Experimental study and steady-state model of a novel plate loop heat pipe without compensation chamber for CPU cooling, Sustain. Cities Soc. 53 (2020) 101894.
[22] S. He, P. Zhou, W. Liu, Z. Liu, Experimental study on thermal performance of loop heat pipe with a composite-material evaporator for cooling of electronics, Appl. Therm. Eng. 168 (2020) 114897.
[23] Y. Aono, N. Watanabe, A. Ueno, H. Nagano, Development of a loop heat pipe with kW-class heat transport capability, Appl. Therm. Eng. 183 (2021) 116169.
[24] W. Ling, W. Zhou, R. Liu, Z. Shen, C. Liu, J. Huang, Experimental investigation of loop heat pipe with novel interlaced microchannel condenser, Int. Commun. Heat Mass Transfer 125 (2021) 105292.
[25] Y.F. Maydanik, S.V. Vershinin, Development and tests of ammonia Miniature Loop Heat Pipes with cylindrical evaporators, Appl. Therm. Eng. 29 (2009) 2297–2301.
[26] A.R. Anand, A. Jaiswal, A. Ambirajan, P. Dutta, Experimental studies on a miniature loop heat pipe with flat evaporator with various working fluids, Appl. Therm. Eng. 144 (2018) 495–503.

[27] R. Zhao, Z. Zhang, S. Zhao, H. Cui, Z. Liu, W. Liu, Experimental study of flat-disk loop heat pipe with R1233zd(E) for cooling terrestrial electronics, Appl. Therm. Eng. 197 (2021) 117385.
[28] Z. Wan, J. Deng, B. Li, Y. Xu, X. Wang, Y. Tang, Thermal performance of a miniature loop heat pipe using water–copper nanofluid, Appl. Therm. Eng. 78 (2015) 712–719.
[29] M. Salarnia, D. Toghraie, M.A. Fazilati, B. Mehmandoust, M. Pirmoradian, The effects of different nanoparticles on physical and thermal properties of water in a copper oscillating heat pipe via molecular dynamics simulation, J. Taiwan Inst. Chem. Eng. 143 (2023) 104721.
[30] K. Jin, Y. Tai, D. Toghraie, M. Hekmatifar, The effects of nanoparticle percentages and an external variable magnetic field on the atomic and thermal behaviors in an oscillating heat pipe via molecular dynamics simulation, J. Mol. Liq. 360 (2022) 119570.
[31] Y.F. Maydanik, S.V. Vershinin, M.A. Chernysheva, Investigation of thermal characteristics of a loop heat pipe in a wide range of external conditions, Int. J. Heat Mass Transf. 147 (2020) 118967.
[32] B. Xiao, W. Deng, Z. Ma, S. He, L. He, X. Li, F. Yuan, W. Liu, Z. Liu, Experimental investigation of loop heat pipe with a large squared evaporator for multi-heat sources cooling, Renew. Energy 147 (2020) 239–248.
[33] G. Kumaresan, S. Venkatachalapathy, L.G. Asirvatham, Experimental investigation on enhancement in thermal characteristics of sintered wick heat pipe using CuO nanofluids, Int. J. Heat Mass Transf. 72 (2014) 507–516.
[34] Z. Zhao, G. Peng, Y. Zhang, D. Zhang, Heat transfer performance of flat micro-heat pipe with sintered multi-size copper powder wick, Case Stud. Therm. Eng. 42 (2023) 102720.
[35] F.H.S. Ginting, A.P. Tetuko, N.S. Asri, L.F. Nurdiyansah, E.A. Setiadi, S. Humaidi, P. Sebayang, Surface treatment on metal foam wick of a ferrofluid heat pipe, Surf. Interfaces 36 (2023) 102499.
[36] W. Zhou, W. Ling, L. Duan, K.S. Hui, K.N. Hui, Development and tests of loop heat pipe with multi-layer metal foams as wick structure, Appl. Therm. Eng. 94 (2016) 324–330.
[37] A.B. Solomon, A.K. Mahto, R.C. Joy, A.A. Rajan, D.A. Jayprakash, A. Dixit, A. Sahay, Application of bio-wick in compact loop heat pipe, Appl. Therm. Eng. 169 (2020) 114927.
[38] B. Weisenseel, P. Greil, T. Fey, Biomorphous silicon carbide as novel loop heat pipe wicks, Adv. Eng. Mater. 19 (2016) 1600379.
[39] K. Nakamura, A. Ueno, H. Nagano, Experimental study on long-distance anti-gravity loop heat pipe with submicron-scale porous structure, Appl. Therm. Eng. 214 (2022) 118793.
[40] Y. Cao, C. Guo, Y. Yu, J. Ma, D. Wu, Y. Zou, Performances of loop heat pipe with the novel bi-porous quaternary MAX phase Ti3(Al, Si)C2 capillary wick, Vacuum 202 (2022) 111185.
[41] X. Li, D. Yao, K. Zuo, Y. Xia, Y.-P. Zeng, Effects of pore structures on the capillary and thermal performance of porous silicon nitride as novel loop heat pipe wicks, Int. J. Heat Mass Transf. 169 (2021) 120985.
[42] J. Esarte, J.M. Blanco, A. Bernardini, J.T. San-José, Optimizing the design of a two-phase cooling system loop heat pipe: wick manufacturing with the 3D selective laser melting printing technique and prototype testing, Appl. Therm. Eng. 111 (2017) 407–419.
[43] J. Xu, D. Wang, Z. Hu, L. Zhang, L. Ye, Y. Zhou, Effect of the working fluid transportation in the copper composite wick on the evaporation efficiency of a flat loop heat pipe, Appl. Therm. Eng. 178 (2020) 115515.
[44] S. He, P. Zhou, Z. Ma, W. Deng, H. Zhang, Z. Chi, W. Liu, Z. Liu, Experimental study on transient performance of the loop heat pipe with a pouring porous wick, Appl. Therm. Eng. 164 (2020) 114450.
[45] Y. Zhang, J. Liu, J.S.i.T.E. Wang, Tao, H. Chen, H. Xue, Experimental study on the characteristics of loop heat pipe with modified carbon fiber felt wick, Appl. Therm. Eng. 234 (2023) 121239.
[46] P. Kumar, M. Gachake, S. Khandekar, Effect of wick oxidation on the thermal performance of a copper-acetone loop heat pipe, Appl. Therm. Eng. 200 (2022) 117627.
[47] N. Phan, Y. Saito, N. Katayama, H. Nagano, Operating characteristics of a dual flat-evaporator loop heat pipe for single heat source cooling in any orientation, Int. J. Heat Mass Transf. 172 (2021) 121146.
[48] N. Phan, N. Watanabe, Y. Saito, S. Hayashi, N. Katayama, H. Nagano, Flat-evaporator-type loop heat pipe with hydrophilic polytetrafluoroethylene porous membranes, Phys. Fluids 32 (2020) 047108.
[49] X. Li, P. Ming, G. Yu, Y. Chen, Z. Tan, Y. Ma, The influence of cone structure and wettability on vaporization nucleation, J. Mol. Liq. 390 (2023) 123080.
[50] H.S. Ahn, C. Lee, H. Kim, H. Jo, S. Kang, J. Kim, J. Shin, M.H. Kim, Pool boiling CHF enhancement by micro/nanoscale modification of zircaloy-4 surface, Nucl. Eng. Des. 240 (2010) 3350–3360.
[51] L. Dong, X. Quan, P. Cheng, An experimental investigation of enhanced pool boiling heat transfer from surfaces with micro/nano-structures, Int. J. Heat Mass Transf. 71 (2014) 189–196.
[52] H. Guo, X. Ji, J. Xu, Enhancement of loop heat pipe heat transfer performance with superhydrophilic porous wick, Int. J. Therm. Sci. 156 (2020) 106466.
[53] Y. Nam, Y.S. Ju, A comparative study of the morphology and wetting characteristics of micro/nanostructured Cu surfaces for phase change heat transfer applications, J. Adhes. Sci. Technol. 27 (2013) 2163–2176.
[54] Z. Zhang, R. Zhao, Z. Liu, W. Liu, Application of biporous wick in flat-plate loop heat pipe with long heat transfer distance, Appl. Therm. Eng. 184 (2021) 116283.
[55] Y. Tan, M. Liu, D. Wei, J. Ren, Y. Wang, H. Jin, S. Shen, Oriented thermal etching of hollow carbon spheres with delicate heat management for efficient solar steam generation, Int. J. Heat Mass Transf. 178 (2021) 121579.
[56] A.K. Singh, N. Yasri, K. Karan, E.P.L. Roberts, Electrocatalytic activity of functionalized carbon paper electrodes and their correlation to the fermi level derived from Raman Spectra, ACS Appl. Energy Mater. 2 (2019) 2324–2336.
[57] M. B, A.M. Raj, G.C. Thomas, Tailoring of low grade coal to fluorescent nanocarbon structures and their potential as a glucose sensor, Sci. Rep., 8 (2018) 13891.
[58] Y. Liu, X. Liu, W. Dong, L. Zhang, Q. Kong, W. Wang, Efficient adsorption of sulfamethazine onto modified activated carbon: a plausible adsorption mechanism, Sci. Rep. 7 (2017) 12437.
[59] D. Wang, Z. Liu, J. Shen, C. Jiang, B. Chen, J. Yang, Z. Tu, W. Liu, Experimental study of the loop heat pipe with a flat disk-shaped evaporator, Exp. Therm Fluid Sci. 57 (2014) 157–164.
[60] M.A. Chernysheva, Y.F. Maydanik, Analysis of the thermal resistance of a loop heat pipe based on the P-T diagram of the working fluid operating cycle, Int. J. Heat Mass Transf. 209 (2023) 124157.
[61] R.J. Mofat, Describing the uncertainties in experimental results, Exp. Therm Fluid Sci. 1 (1998) 3–17.
[62] A.R. Anand, A. Ambirajan, P. Dutta, Investigations on vapour blanket formation inside capillary wick of loop heat pipe, Int. J. Heat Mass Transf. 156 (2020) 119685.
[63] S.-C. Wu, Z.-H. Lin, S. Lo, W.-J. Lin, Effect of PTFE wick thickness on Loop heat pipe performance, Therm. Sci. Eng. Prog. 42 (2023) 101911.
[64] Z. Liu, H. Li, B. Chen, J. Yang, W. Liu, Operational characteristics of flat type loop heat pipe with biporous wick, Int. J. Therm. Sci. 58 (2012) 180–185.